Magnetic Field Sensing via Multi-Material Acoustic Sensing Optical Fibers with Magnetostrictive Cladding Inclusions

Zach B Dejneka

Thesis submitted to the faculty of the Virginia Polytechnic Institute and State University in partial fulfillment of the requirements for the degree of

Master of Science

In

Materials Science and Engineering

Gary R. Pickrell- Chair

Daniel S. Homa

Anbo Wang

February 2, 2024

Blacksburg, VA

Keywords: Magnetic Sensing, magnetostriction, vibration, distributed acoustic sensing, optical fiber

Magnetic Field Sensing via Acoustic Sensing Fibers with Magnetostrictive Cladding Inclusions

Zach B Dejneka

Abstract

In this conducted research, optical fiber sensors are used to measure low strength alternating magnetic fields. Various fiber sensor configurations are tested and investigated to demonstrate sensing capabilities at different field magnitudes and frequencies. Distributed acoustic sensing fibers (DAS) have been largely studied and documented across a variety of applications and sensing systems. This research uses the DAS technology in tandem with magnetostrictive materials to create a distributed multi-material optical fiber magnetic sensor.

Magnetic sensing has high demand across different fields and often runs into challenges of extreme environments including high temperature, corrosion, and areas with poor accessibility. The robust and distributed nature of optical fiber sensors which can be cheaply produced for long lengths is an attractive option over other single point magnetic sensors. In down hole applications specifically, having a distributed sensor able to be deployed easily and over long distances for magnetic sensing would be a large improvement to bulkier traditional magnetometers.

In the conducted study, different magnetostrictive materials are implemented in distributed optical fiber sensors to analyze and compare the effective sensitivity and potential commercial viability. Nickel, galfenol alloy, and MetGlas alloy inclusions are drawn into fused silica optical fibers with Bragg gratings inscribed later on for DAS capability. Each was investigated for its response to varying AC magnetic fields to determine relative sensitivity and resolution for distributed magnetic field sensing.

Magnetic Field Sensing via Acoustic Sensing Fibers with Magnetostrictive Cladding Inclusions

Zach B Dejneka

General Audience Abstract

Magnetic sensing has high demand in biomedical applications as well as within the oil and energy industry. This research proposes a series of optical fiber-based sensors to overcome many of the challenges present amidst traditional magnetic sensors. Materials that respond to magnetic fields by either contracting or expanding are coined magnetostrictive. The proposed fiber-based sensors use magnetostrictive materials to create a change in the optical path length of the light being transmitted through the optical fiber. This path difference can be converted to a strain measurement and when compared with a standardized magnetometer, a calibration curve is established for the fiber sensor.

Different magnetostrictive materials are studied for measuring various alternating magnetic field amplitude strengths to look at improved sensitivity and/or resolution. This includes nickel, galfenol alloy, which is made up of iron and gallium, and MetGlas, which is composed of primarily of iron. Small wires of the respective materials are drawn out inside the silica fiber while the optical fiber is made so that continuous lengths run the course of the fiber. Different sizes were experimented with. Another simplified tested setup used a ribbon of the MetGlas while a distributed acoustic fiber sensor was laid on top to pick up the strain response while exposed to an alternating magnetic field.

All of the mentioned test setups showed success in measuring alternating magnetic field strengths with a clear positive correlation of strain response to magnetic field amplitude. A

calibration curve was established for each sensing system and analyzed to show an effective sensitivity range.

Acknowledgements

I would like to acknowledge my committee members for their help, knowledge, and guidance surrounding my graduate work at Virginia Tech. I would like to thank Dr. Gary Pickrell for asking the right questions to help me think critically and how to improve upon my own work and development as a student. Being able to rely on Dr. Pickrell's experience and knowledge was of great benefit. I would like to thank Dr. Dan Homa for the constant support and generation of ideas. Without him, I would not have been able to accomplish nearly as much as I did for my Master's work. Being able to always talk out problems and struggles surrounding theory, experimentation, and writing was incredibly helpful. Lastly, I would like to thank Dr. Anbo Wang for his encouragement and positive feedback on my work making it that much easier to be excited about the research. I also greatly appreciate his expertise in fiber optics and the use of Sentek Instrument technology, without which, this work would not have been possible.

I would also like to thank my fellow peers in the research group and outside of it for helping with the testing, data analysis and generation of ideas throughout my project work. Gideon Crawford and Josh Buontempo made the work more enjoyable and provided valuable sounding boards for discussing the various obstacles that research often creates. Steve McCartney at the nanoscale fabrication lab provided invaluable assistance with working the SEM and being able to characterize the fiber samples I worked with, and I greatly appreciate his help.

Table of Contents

Table of Figures

Introduction

Optical fiber has revolutionized interconnectivity and communication across the world. Fiber optic technology has allowed us to transmit large amounts of data across vast distances and is the reason why we are able to rely on the internet across the globe. All of this transmitted information travels while operating at the speed of the light contained within the fused silica of the fiber drawn out to the width of a human hair. The development of fiber optic technology has given rise to sensors and detection systems based in fiber optic cables. [1-4]

Magnetic sensors are also playing an increasingly more prevalent role in modern society. The detection of very weak magnetic fields permits brain and heart imaging, while sensor arrays enable subsurface geophysical characterization for oil and gas production, as well as carbon storage. Superconducting quantum interference devices (SQUIDs) are used in Magnetic Resonance Imaging (MRI) for Magnetoencephalography (MEG), but their size, cost, and requirement for cryogenic cooling have limited their widespread clinical use [1-3]. Fluxgate magnetometers (FGMs) and nuclear magnetic resonance (NMR) sensors are used in downhole applications [1], but are also very bulky, sensitive to electromagnetic interference (EMI) and have nontrivial power requirements [4-5]. As such, there has been significant interest in the development of magnetoelectric (ME), magnetoresistive (MR), Hall effect, and giant magnetoimpedance (GMI) sensors with the performance and attributes necessary for these applications. However, each are susceptible to EMI, require electrical power and are not easily configured for multiple measurements [6-9].

Optical fiber technologies have the potential to meet demand for magnetic sensors that can remotely detect magnetic fields with high spatial resolution, while maintaining a small footprint with minimal power requirements. A wide variety of fiber optic sensors based on fiber Bragg gratings (FBGs), long period fiber gratings (LPFGs), Fabry Perot interferometers (FPIs), Mach Zehnder interferometers (MZIs), Sagnac and Michelson interferometers, evanescent field detection, and detection of changes in polarization state have been used in sensing applications [2][10-11]. Although magnetically sensitive materials like ferrofluids and magneto-optical crystal such as yttrium iron and rare earth garnets have found success, those based on the transduction of strain to optical fiber via included magnetostrictive materials possess the most promise.

Background

1. Optical Fiber Based Sensing

Telecom single mode fibers (SMF) most frequently operate using light with a wavelength of 1550 nm but also can use wavelengths of both 850 and 1310 nm depending on the application. These specific wavelengths are chosen due to their low attenuation. Absorption from impurities in the glass and specifically from water vapor is lower at these points allowing minimum attenuation and loss [2][5-7]. Fiber optic sensing technology relies on measuring optical path differences (OPD) and interference for a given transmitted wavelength of light called interferometry. A signal sent through a fiber cable has an expected optical path as the wavelength and refractive index of the light and material are known. This optical path is susceptible to changes such as bending and strain which physically change the path length. An OPD is also influenced by changes in refractive index derived from things such as temperature and stress. [6][8-11]

In this study, fiber Bragg gratings (FBG) are used so that an OPD can be measured. FBG sensors are a well-known and reliable sensing technology closely studied in the literature to record strain measurements using optical fiber [2-3][12]. FBG sensors work by periodically altering the refractive index along the length of the fiber by means of a femtosecond laser. Every two meters along the length of the optical fiber, an FBG is inscribed with a periodic exposure of the fiber core to the laser. At each segment of cyclic refractive index change, some of the light is reflected through the core at a specified wavelength. The reflected wavelength, λ_B, is given by the equation:

$$\lambda_B = 2n_c\Lambda \tag{1}$$

Where n_c is the fiber core refractive index and Λ is the period of the Bragg grating. An interrogation system monitors the reflected light. External stimuli apparent on the fiber create small deviations in the wavelength of the propagating light. These deviations correspond to a change in effective optical path length and can be converted to a strain measurement. Wavelength changes can be affected by stress, bending of the fiber, temperature, or strain. In this study, the stress and caused strain on the fiber from the magneto-striction of wire inclusions in the fiber cladding is tested and analyzed as temperature and fiber position are maintained.

Because there is an expected time domain for the reflected light to be received from each period grating, there will be a location along the fiber associated with each OPD. This allows for the distributed acoustic sensing or DAS for these fiber sensors.

2. Magnetostrictive Materials and Optical Fiber Sensing

In this study, nickel, MetGlas alloy, and galfenol alloy are drawn into the fused silica optical fiber during the draw process in different configurations. These materials experience lattice stress upon subjection to an external magnetic field. The corresponding strain response is induced by magnetic domains in the metal materials aligning to the field [3-5]. This phenomenon called magnetostriction is given by the linearized equation (ignoring any effects from temperature):

$$\varepsilon = \frac{\sigma}{E_{\gamma}^{H}} + d_{33}H \tag{2}$$

where ε is the strain response, σ is the resultant stress, E_{γ}^{H} is the elastic modulus dependent on the applied magnetic field, H, and where d_{33} is the magneto-mechanical coefficient of the material.

The maximum strain response from the magneto-striction of the material is determined by the initial positioning of the magnetic domains in the metal alloy. The wires contained inside the magnetic sensing fiber sample have randomly oriented magnetic domains. When an external magnetic field is applied, the domains align with the axis of the field as shown in Figure 2-1 which results in the strain response (magneto striction). The saturation magnetic field strength occurs when the strain response is at the maximum. Once the domains are completely aligned with a magnetic field, no further straining of the material can occur. For a given length of magnetic domains as pictured, the change in span between the randomly aligned domains to the domains all ordered axially with the saturation magnetic field strength is λ.

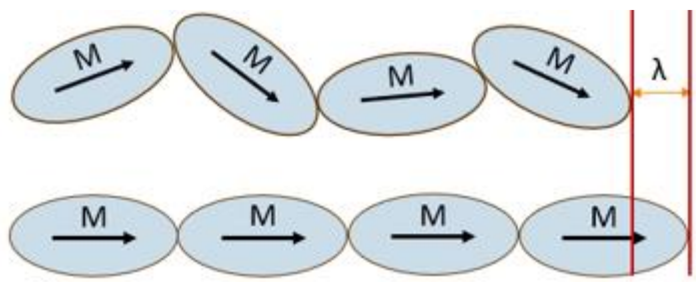

Figure 2-1: Magnetic domain alignment in a magnetostrictive material.

The magnetostrictive response to an AC magnetic field undergoes a frequency doubling effect due to the nature of the magnetic domains in the material [13]. Regardless of whether the field is oriented to the positive direction of a given axis, or the negative, the maximum strain response (all domains are orderly aligned as in Figure 2-1) and effective initial lattice positioning remain the same. This gives a frequency doubling in the strain response compared to the driving frequency of the alternating magnetic field. A given strain response from a magnetic field with an amplitude of A will have the exact same strain response where the field amplitude is $-A$. This is shown in Figure 2-2. However, if an offset or bias is applied to the magnetic field such that the midpoint of the sinusoidal AC signal is no longer zero, a frequency shift will occur [8][14]. This is because the maximum magnetic field and the minimum magnetic field strength of an AC signal no longer correspond to the same strain response. As the bias / offset is increased, the strain response will shift to a combination of decreasing doubled magnetostrictive behavior frequency response and an increasing driving frequency response from the material. Once the offset is such that the minimum magnetic field strength is greater than zero, the strain response will only be composed of the driving frequency as shown by the dotted line in Figure 2-2.

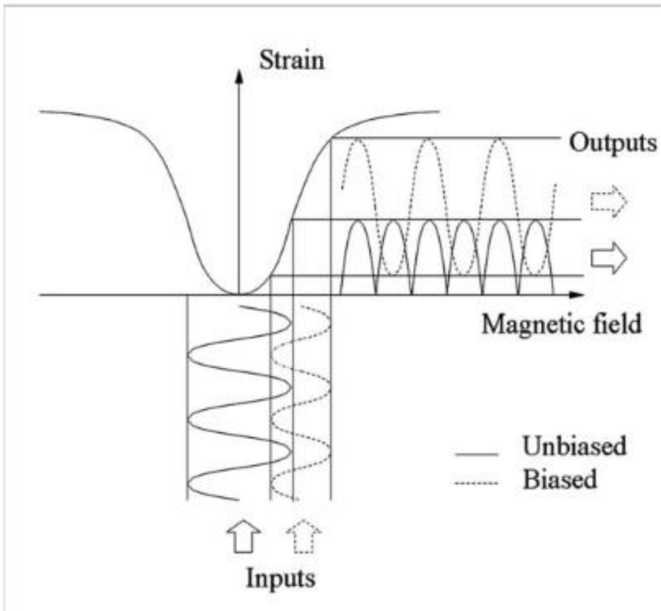

Figure 2-2: General magnetostriction curve and biasing effects of strain versus magnetic field.

Magnetostrictive metal inclusions drawn inside a fused silica fiber sample allow for AC magnetic field induced strain response to transfer to the cladding and core of the fiber. This causes an OPD which can then be measured using FBG’s and interferometry. The fiber optic magnetic sensors produced, tested, and analyzed in this study function using this system.

3. Thermal Magnetic Annealing

Figure 1 demonstrates the effective strain response in a magnetostrictive material when exposed to an external magnetic field. However, the strain response can be altered and even improved with thermal magnetic annealing. The maximum magnetostrictive strain response is determined by the initial positioning of the magnetic domains in the metal alloy [19]. The magnetic domains in the respective material begin as randomly positioned. When an external magnetic field is applied, the domains align with the axis of the field as shown in Figure 3-1(a) and elicit the strain response. For a given magnetic domain's length, the change in span between the randomly aligned domains to the domains all ordered axially with the saturation magnetic field strength is λ. However, if these domains are positioned entirely perpendicular to the later applied field, the effective span, λ_a, increases the maximum strain, as shown in Figure 3-1(b). This can be done by applying a DC magnetic field across the magnetostrictive material, perpendicular to the intended AC magnetic field axis. However, the effect is not permanent.

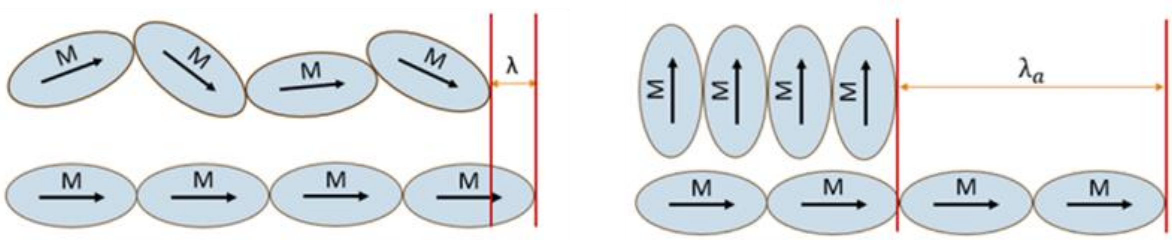

(a) (b)

Figure 3-1. (a) Magnetic domain alignment in a randomly oriented magneto strictive sample (b) Perpendicular magnetic domain alignment in a DC magnetic field biased material with strain response λ.

Thermal annealing a magnetostrictive alloy with an applied DC magnetic field ensures that the realignment, and improvement in the strain response, is more permanent. This is done by heating up the metal, above the Curie temperature, while the perpendicular field is applied. Upon cooling, the magnetic domains are “locked in’ their new alignment. [20-21]

Materials and Methods

In this research, multiple fiber sensor configurations are studied and analyzed. Different approaches to the configurations are implemented to deal with obstacles and shortcomings associated with the initial tests and look at ways of altering the effective sensitivity of a fiber sensor. Two unique processes were used to fabricate the multi-material fiber optic sensor samples. The first method looked at multi-material fiber sensors with one or two magnetostrictive inclusions on the order of ~ten microns in diameter.

4. Magnetic Sensing Optical Fiber Fabrication

The first rendition of the multi-material single mode optical fiber sensor was fabricated via a vacuum assisted stack and draw technique. Fused silica rods were arranged inside an external preform concentrically around a germania doped silica core rod as shown in Figure 4-1. Two of the rods were replaced with fused silica tubes and then filled with nickel powder.

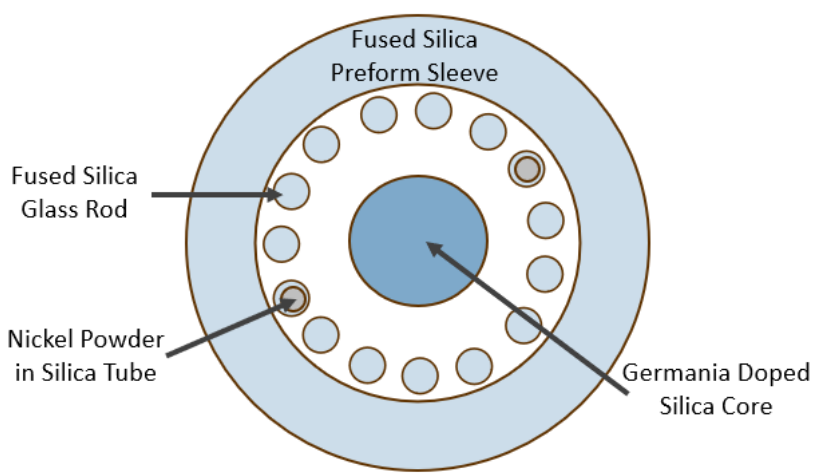

Figure 4-1: Fused silica preform arrangement for a nickel double wire multi-material fiber sensor.

The preform was assembled and fiberized using the nickel cladding wires as shown in the above image. Using a fully functional 3-story fiber draw tower, the optical fiber preform was heated in a furnace and pulled under tension to the desired diameter of 125 microns. The fiber is run through a die with acrylate coating and then spooled. The fused silica preform draws alongside the nickel filled tubes and core rode such that the initial ratios are maintained, and continuous nickel inclusion wires run the entire length of the drawn fiber.

A second variation of the larger cladding wire sample sensor was produced using MetGlas® 2605C which is a magnetostrictive alloy specifically engineered for high strain response for lower externally applied magnetic fields. Additional processing was required to create MetGlas® 2605C wires with diameters on the order of 1 to 2 millimeters for insertion in the preform stack. The MetGlas® 2605C ribbon was cut into pieces and inserted in a fused silica glass tube and drawn into glass encapsulated wire. The glass encapsulation was mechanically removed and the MetGlas® 2605C wire was inserted into a fused silica capillary tube and included in the preform stack that was fiberized on a commercial scale fiber optic draw tower with an acrylate coating [19] the same way as the nickel multi-material fiber sensor.

Weakly reflecting broadband FBG's were then inscribed and fabricated in the fiber via a 780nm infrared- femtosecond (IR-fs) laser. The cyclic IR-fs laser contacts the core of the fiber, and a periodic refractive index change is induced as shown in the circled FBG in Figure 4-2 with a grating period of 900nm. When incident light transmits through the fiber and grating at an initial wavelength of 1550nm, a wavelength change upon reflection at the FBG occurs with a Bragg wavelength of 529nm [14]. The gratings are inscribed every two meters to function as distributed

Fabry-Perot interferometers. The fiber was positioned so that the laser has an open path to the core without being obstructed by the nickel or MetGlas® wires for each sample.

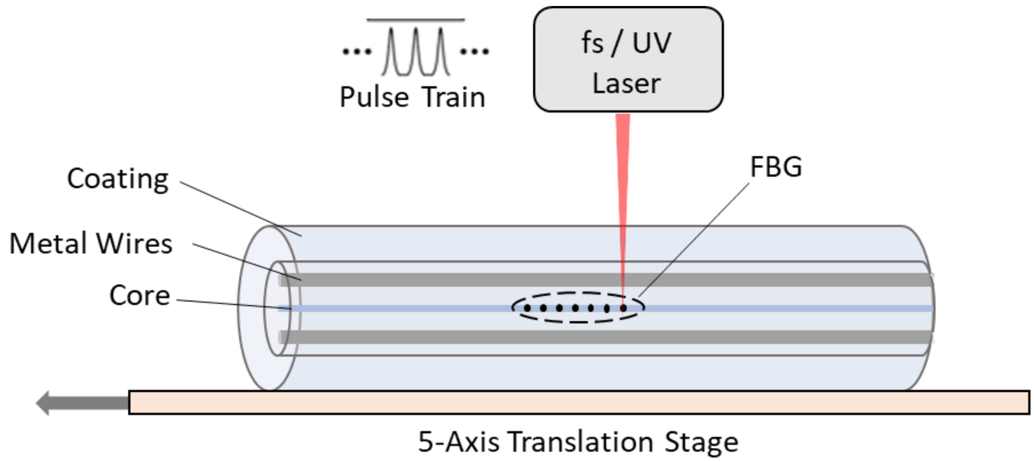

Figure 4-2: Broadband fiber Bragg grating inscription setup with a femtosecond laser using the point-by-point method.

The second variation of the multi-material optical fiber sensor used nickel or galfenol alloy to introduce sub-micron diameter magnetostrictive inclusions inside the fiber cladding. The multi-material optical fiber was also fabricated via a vacuum assisted stack and draw process on a commercial scale fiber optic draw tower [14]. First, the fused silica tubes were filled with nickel powder or pieces of galfenol wire and drawn into canes (diameters on the order of 2 to 3 millimeters) via the melt-draw technique. These canes were then stacked into another fused silica tube and drawn into canes with a similar diameter. These canes were again stacked into a fused silica tube around a core rod that consisted of single mode core and fused silica cladding. The preform was then fiberized, coated with an acrylate, and spooled.

As shown in Figure 4-3, weakly reflecting broadband FBGs were similarly fabricated. This inscription process is identical to the one used for the larger inclusions in Figure 4-2, but the orientation of the fiber was no longer relevant as the inclusions were small enough that they did not interfere with the writing process.

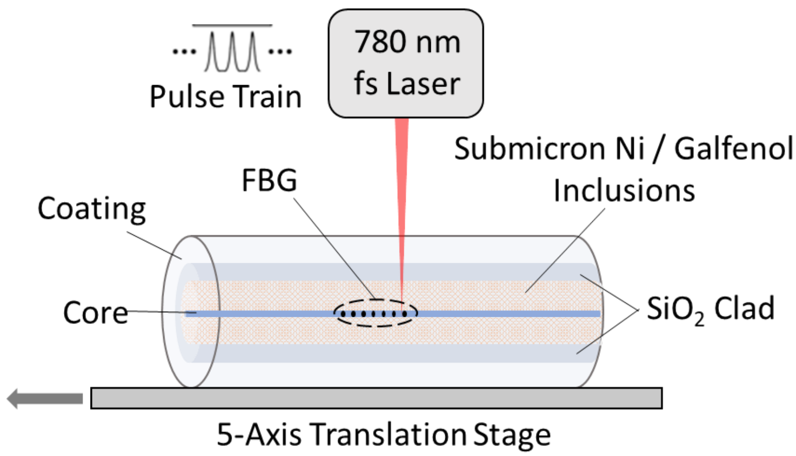

Figure 4-3: Fiber Bragg grating inscription by means of a femtosecond laser in magnetic sensing fiber.

5. Material Characterization

Following the FBG inscription of the magnetic sensing fiber, the samples were then characterized using a scanning electron microscope (SEM, LEO 1550). The samples were cleaved, and any fracture debris was removed with compressed air. Using conductive carbon tape, the fractured samples were adhered to a metal mount and sputter coated with 10nm of Pt/Pd so to be conductive for SEM analysis and imaging. Secondary electron detector (SED) and backscatter electron detector (BSD) images were taken of multiple samples of the 10-micron diameter nickel wire fiber, submicron nickel wire sample and the Metglas® 2605C variants.

A quant map was then created using energy dispersive X-ray spectroscopy (XPS) looking at concentrations of nickel, silicon and germanium (the fiber core is silica doped with germanium). Figure 5-1 depicts the SEM BSD image as well as the XPS map.

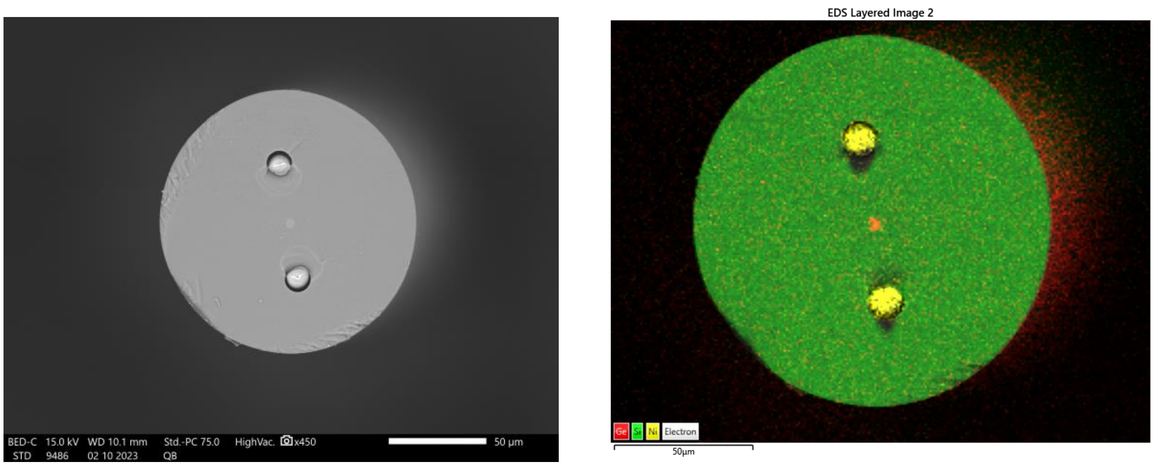

Figure 5-1: SEM BSD image and XPS map of two nickel wire multi-material fiber sample.

This shows the size of the wires relative to the fiber dimension. It also demostrates that the nickel inside the fiber is not bonded to the fused silica. During the draw process, the coeffecient of thermal expansion (CTE) of silica is much lower than that of nickel. Because of this, upon cooling after the fiber draw, the metal shrinks while there is little dimensional change in the silica cladding. This leaves a small gap between the wires and the cladding. This phenenomena is present across all the fiber samples even with smaller inclusions which is discussed later.

The second sample that was tested was nearly identical to the first but instead only used a single nickle wire. This makes the FBG writing process easier. To get to the core of the fiber with the femtosecond laser for grating inscription, the fiber has to be oriented so that the metal wires are not in the way otherwise the metal will reflect and absorb the laser. Hence, a single wire makes the writing process significantly easier especially considering the relative diameter of the nickel in comparison to the entire fiber width. The BSD single wire nickel fiber SEM image also taken at 15kV is depicted in Figure 5-2.

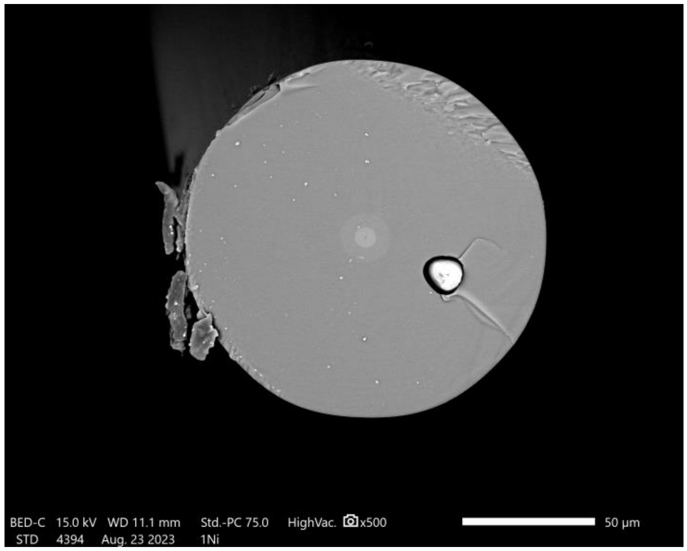

Figure 5-2: SEM BSD image of single wire nickel multi-material fiber sample.

MetGlas alloy was used after the nickel samples to try to improve relative sensitivity which is discussed in the results and discussion section. In Figure 5-3, a single wire MetGlas fiber sample is shown looking at a closeup of the contained cladding wire at 2500x magnification again demonstrating the gap between the metal and the cladding of the fiber. The corresponding XPS quant map of the fiber looks at concentrations of iron and cobalt (main components of the MetGlas alloy) as well as silicon and germanium.

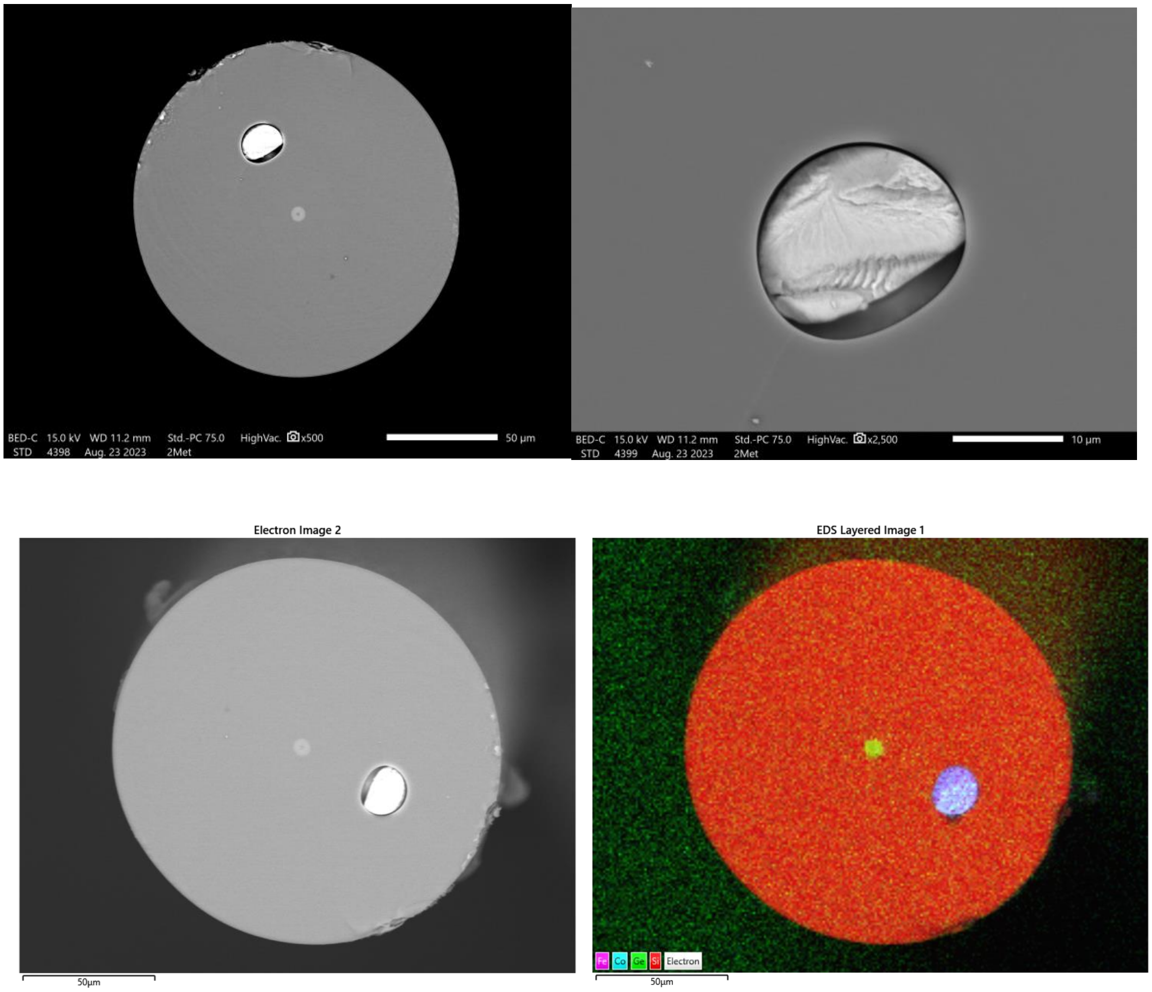

Figure 5-3: SEM BSD image and XPS map of single wire MetGlas multi-material fiber sample.

The XPS quant map displays the strict elemental distribution between the core (composed of silica and germanium), the silica cladding, and the MetGlas inclusion.

As shown by the backscattered image in Figure 5-4, a second sample of single MetGlas® 2605C wire is contained in the fiber cladding centered between the core and the surface of the fiber. The germanium doped fused silica core is clearly visible in the elemental dot map in Figure 5-4 (right). The single MetGlas® wire is identified by the distinct and elevated concentration of iron (yellow) in the fused silica (silicon: green) cladding.

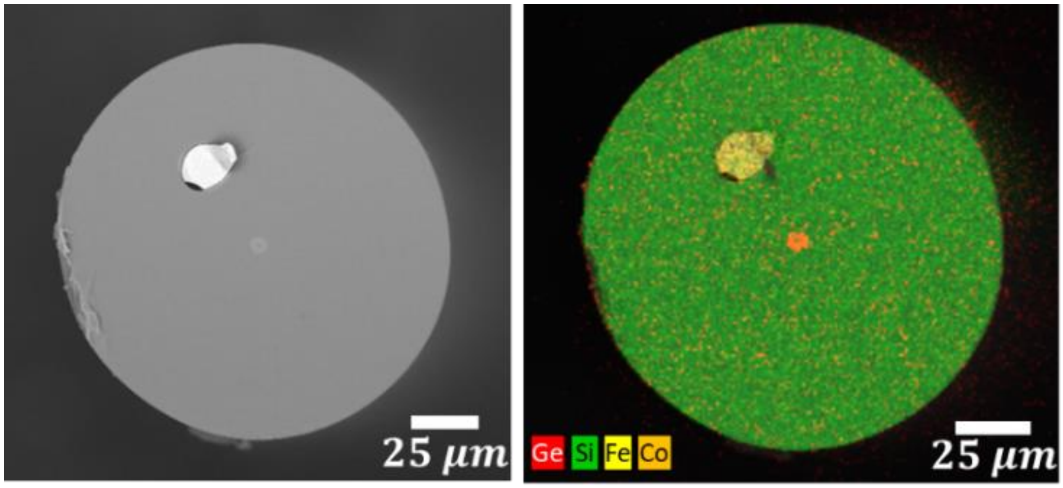

Figure 5-4: SEM backscatter diffraction image and EDS dot map of a single MetGlas® wire cladding magnetic sensing fiber sample.

The cross sections of another two-nickel wire magnetic sensing fiber sample are shown in Figure 5-5. The diameters of the two nickel cladding wires in the fiber shown in Figure 5-5(a) are clearly different. This non-uniformity was due to instabilities that occur during the startup of the fiber draw process. Upon stabilization of the draw wire process, the nickel wires with the same diameter are drawn in the fiber cladding, as shown in Figure 5-5(b).

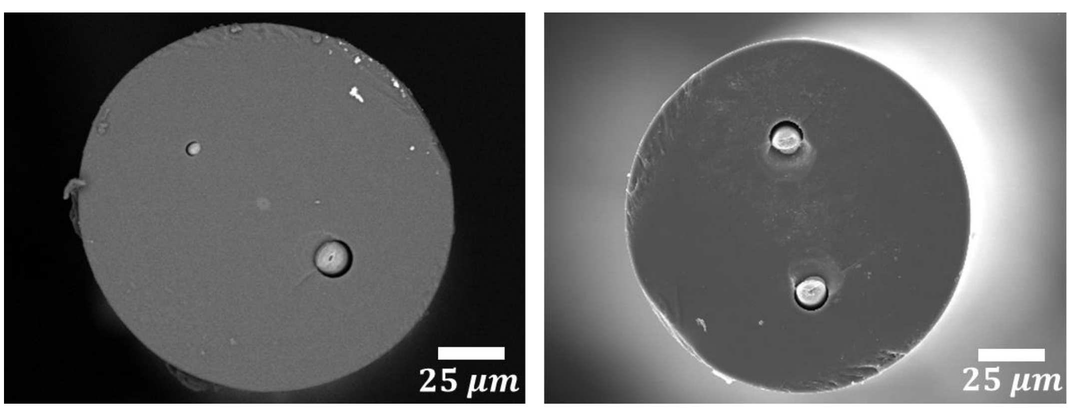

(a) (b)

Figure 5-5: SEM BSD images of two different large wire nickel multi-material magnetic sensing fiber samples at 450x mag.

The sub-micron nickel inclusion samples were then also characterized similarly. In Figure 5-6, BSD images are shown at different magnifications depicting the different nickel inclusion sizes on the sample.

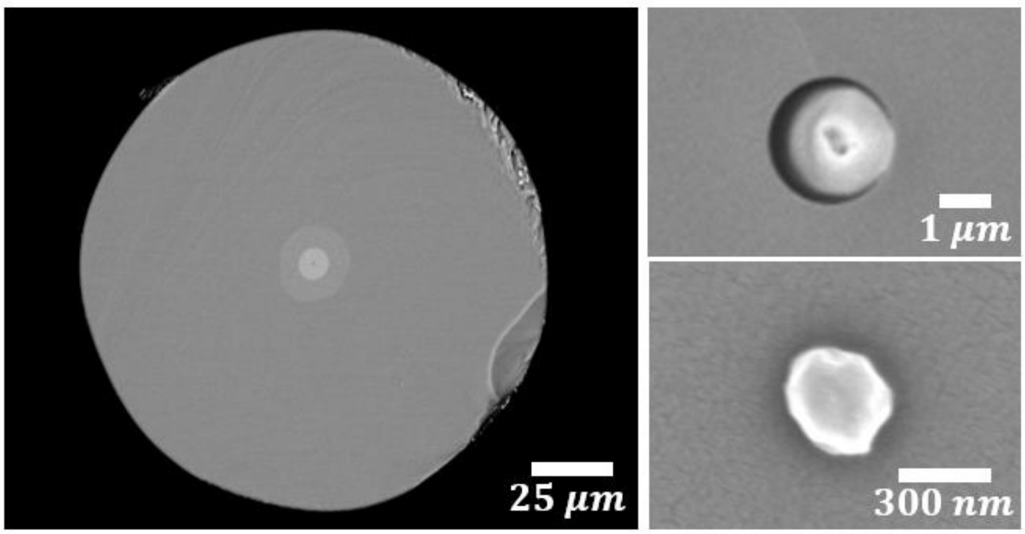

Figure 5-6: SEM BSD images taken at 450x magnification 18000x, and 75000x respectively of nickel inclusions.

Energy-dispersive X-ray spectroscopy (EDS) was performed on a submicron nickel inclusion sample image to analyze the micro-scale chemical composition. From the produced spectrum in Figure 5-7, spectrum one shows a majority weight percent of nickel indicating the wire to be composed of nickel. The remaining weight percent is caused by the resolution of the EDS given the 18000x magnification and possible small introduction of surface debris (carbon and oxygen). The EDS, while not highly accurate in the recorded percentages, is still able to give a reasonable depiction of what is present in the sample demonstrating the bright spots amidst the silica is indeed composed of nickel.

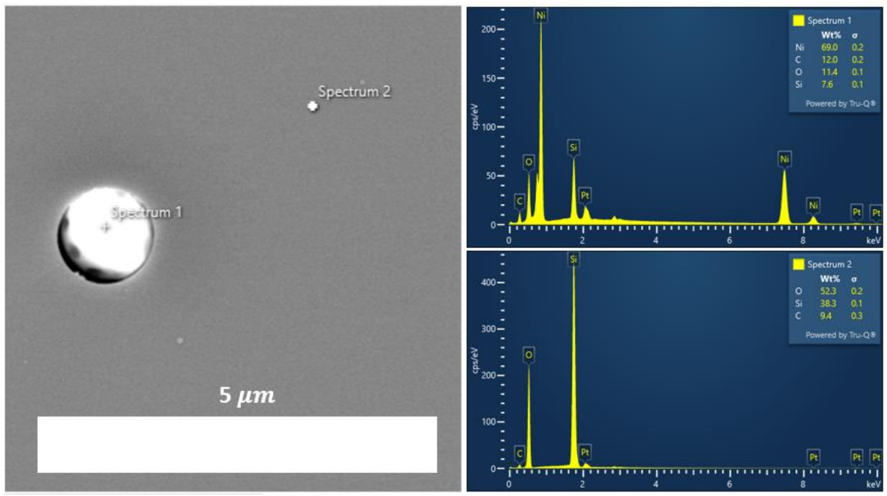

Figure 5-7: EDS spectra looking at nickel and silicon within the fiber sample to demonstrate presence of inclusions.

Comparing this to the larger two nickel wire sample in Figure 5-1, the wires present are at least an order of magnitude smaller but appear to still be unbonded to the fused silica glass. The smaller size allows for splicing capability of the fiber sensor without having warpage from larger metal wire diameter inclusions in the cladding.

6. Optical Fiber Sensor Interrogation

The dynamic strain experienced by the sensing fiber was measured in the time domain with Sentek Instrument’s picoDAS interrogator at sampling frequency of approximately 37 kHz [14]. The weakly reflecting broadband FBGs inscribed in the sensing fiber are paired to form distributed

Fabry-Perot interferometers that are interrogated to provide strain measurement with ultra-high sensitivity (<0.25 nε). The interrogator operates using 1550 nm distributed feedback laser diode with 10 ns pulses. The pulses transmit by means of a 3-port optical circulator that is then connected to the optical fiber. The FBG's inscribed in the sensing fiber partly reflect the incident light at the Bragg wavelength to be received through the circulator by a photodetector. The resultant analogue signals are transformed to digital and are then later processed.

The magnetostrictive inclusions in the fiber induce a strain and vibration in the fiber upon exposure to an AC magnetic field. A refractive index change and OPD is then induced. The OPD is detected by the interrogator through photodetector time deltas in the received FBG reflected light. The strain data from the picoDAS system was analyzed using a MATLAB script and Fast Fourier Transform (FFT). The FFT takes the recorded 3-dimensional (time, distance, and strain) matrix data from the interrogation system and creates an intensity spectrum over a frequency range from 0 to 20000 Hz. The intensity measurement is derived from the amplitude of the sinusoidal constituent for a given frequency.

7. Performance Testing

An air-core solenoid was used to evaluate the response of the sensing fibers upon exposure to lateral magnetic fields. The magnetic sensing fiber was run through the 2-meter-long air core solenoid positioned so that the FBGs were placed at each respective end to maintain the spatial resolution of the fiber. A waveform generator and amplifier were then used to produce magnetic fields over a variety of frequencies and strengths. The corresponding magnetic field strength was characterized by a calibrated magnetometer probe.

When testing the sensing fibers with the larger inclusions (~10-micron diameter nickel and MetGlas), a "mechanical splice" or physical alignment needed to be implemented, as shown in Figure 7-1. To successfully perform the measurements, the picoDAS interrogator was coupled first to a standard telecom fiber "pigtail". The telecom fiber "pigtail" then must be connected to the sensing fiber. This was attempted by using a fusion splicer and manually aligning the fibers. If a fusion splice was attempted, the larger metal wire fiber would warp when trying to establish a fusion splice connection. To get around this, the mechanical splice was performed by having the two fiber ends to be connected first cleaved and checked for a flat surface and exposed core.

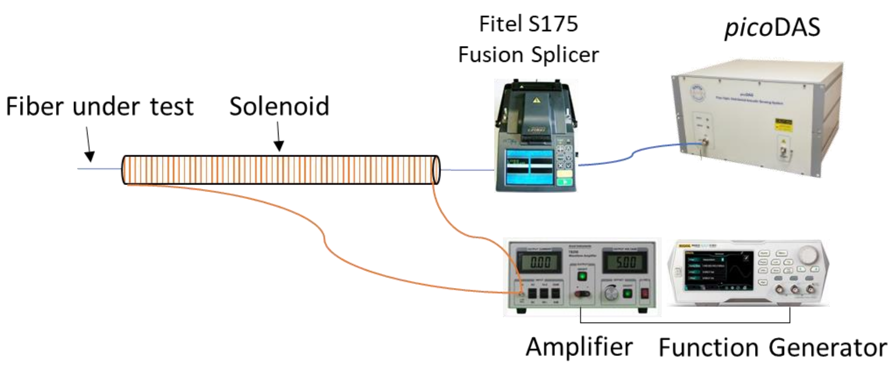

Figure 7-1: AC magnetic field fiber sensing setup with fusion splicer, waveform source, and picoDAS interrogation.

The sensing fiber and "pigtail" were placed into the fiber slots with a drop of index fluid placed on one end. They were then manually aligned and pushed together. An OTDR was used to minimize the effective loss from the "mechanical splice." The process of manual alignment is tedious and time consuming. However, the sensing fiber with submicron nickel cladding wires was easily fusion spliced to a single mode "pigtail" that was connected to the picoDAS simplifying the entire setup process. The submicron nickel inclusions were sufficiently small enough that fiber cleaving was unaffected, and no core warpage occurred during the fusion process.

The MetGlas sensor samples were tested and characterized in the same manner as the single and double nickel wire sample. However, a magnetic sensing fiber with one MetGlas® 2605SC cladding wire was thermally annealed to evaluate the performance improvement by increasing the maximum strain response in the magnetostrictive material. This was done by taking the sensing fiber (~ 2 m) and routing it in a 19x25 mm borosilicate tube wrapped with high temperature heating tape that was positioned in the center of a rectangular Helmholtz coil, as shown in Figure 7-2. The entire structure was supported by an aluminum I-beam with a length of 2.2. meters and width of ~0.6 cm.

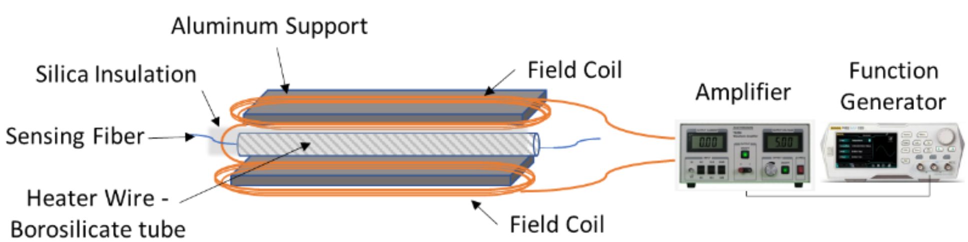

Figure 7-2: Heating coil and DC magnetic field biasing setup for annealing the MetGlas® wire inside the multi-material optical fiber sensor.

A DC voltage was applied across the coil generating a magnetic field of roughly 200 μT perpendicular to the fiber axis. A thermocouple was used to monitor the temperature inside the insulated aluminum channel and a temperature of ~ 400ºC was achieved, maintained for an hour, and then cooled back to room temperature. This is done all while the DC magnetic field was applied to lock the magnetic domains of the MetGlas in place such that they are perpendicular to the field from the air-core solenoid testing setup.

Results and Discussion

Once the fiber samples were subjected to an increasing AC magnetic field amplitude, the corresponding strain response from the dasNOVA interrogation system was processed to yield an intensity frequency spectrum to characterize the sensors in relation to the applied field amplitude. Figure 16 shows one such FFT intensity measurement from a double wire MetGlas sample and the corresponding peaks in relation to the driving frequency used in the air core solenoid generating the AC magnetic field.

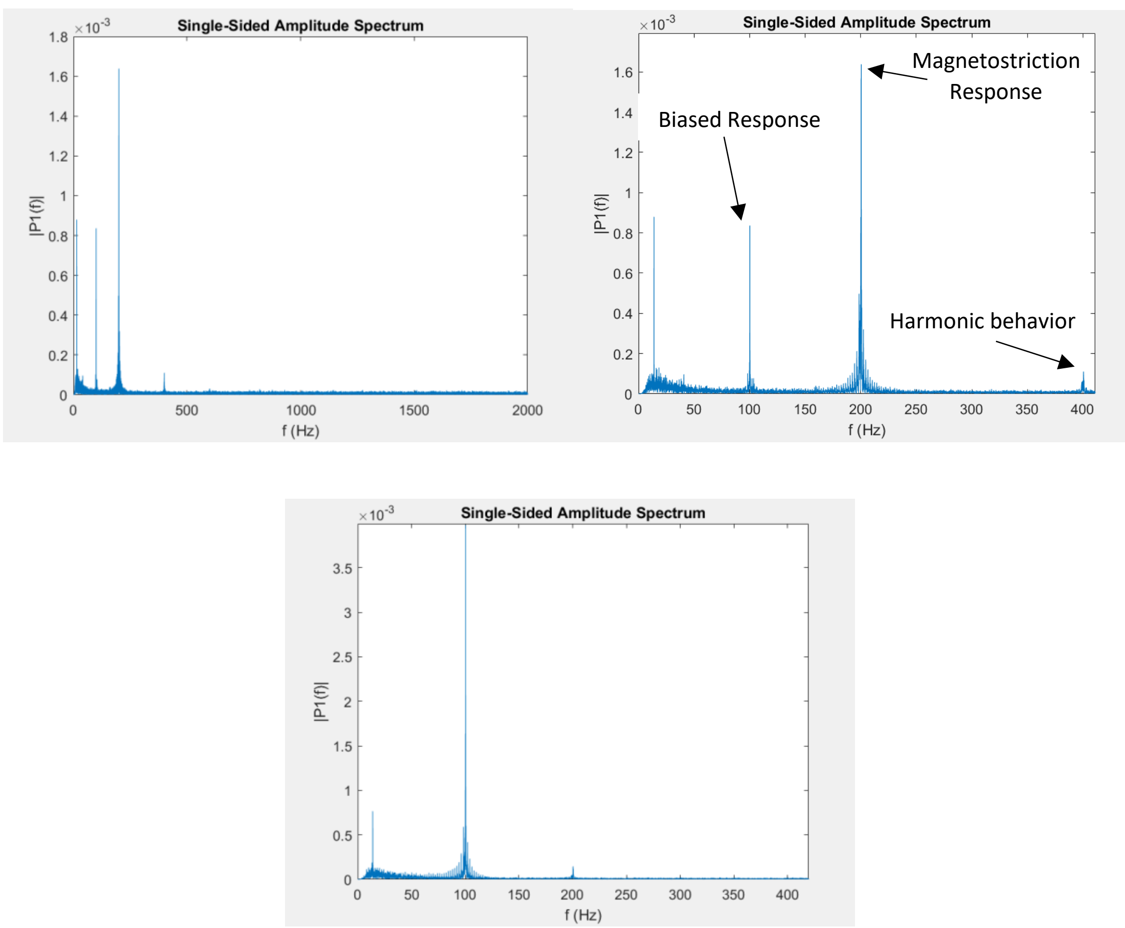

Figure 7-3: Amplitude spectrum response of double wire MetGlas sample at 11.40µT and 5.71µT.

The top left shows the present response peaks from zero to 2000 Hz and the right shows the zoomed in display of the same test at 11.40 μT amplitude for a 100 Hz driving frequency. In this response the doubled magnetostrictive response is most prevalent but at roughly half the magnetic field strength with a 5.71 μT amplitude, the 100 Hz peak dominates. This results from a bias shifting the strain response along the magnetostrictive curve shown in Figure 2-2. However, when the applied AC field is higher, the doubled frequency shows up predominantly. There is also a small peak at 400Hz at the higher field which is a result of an acoustic harmonic from the strain/vibration response. In the lower frequency range, there are some mixed signals coming from noise in the testing environment. In the following presented findings, the strain response is plotted against increasing magnetic field amplitudes across various driving frequencies using different testing setups and magnetic sensing fiber samples. This data is analyzed and discussed, looking at improvements on different fiber materials and sensing configurations.

8. Analysis of Sub-micron Inclusion Sample Data

The first sample tested in this research is the sub-micron nickel inclusion fiber sensor. After successfully splicing the submicron magnetostrictive cladding inclusion sensing fiber to a single mode “pigtail” and setting up the air core solenoid, the sample was exposed to a ramping AC magnetic field. The waveform generator was set to a frequency of 100 Hz and turned on. A step test was performed in increments around 250 μT up to just over 2mT and the corresponding strain data was recorded. The strain data from the picoDAS system was analyzed using a MATLAB script and Fast Fourier Transform (FFT). The FFT intensity of double the waveform driving frequency (magnetostrictive strain response occurs at twice the driving frequency) was plotted against the AC magnetic field of the air core solenoid as shown in Figure 8-1.

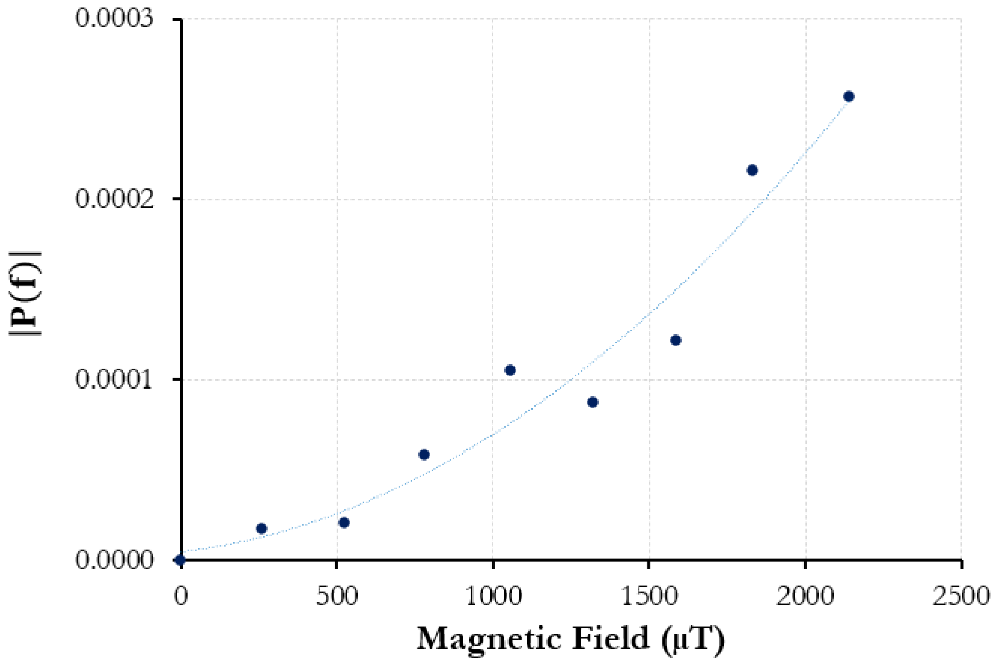

Figure 8-1: Submicron nickel inclusion fiber 200Hz amplitude spectrum intensity vs 100 Hz AC magnetic field amplitude.

The micron sized nickel wire inclusions, when exposed to a periodic magnetic flux vibrate at double the frequency of the waveform generator in a second calibration test done at 170 Hz as shown in Figure 8-2.

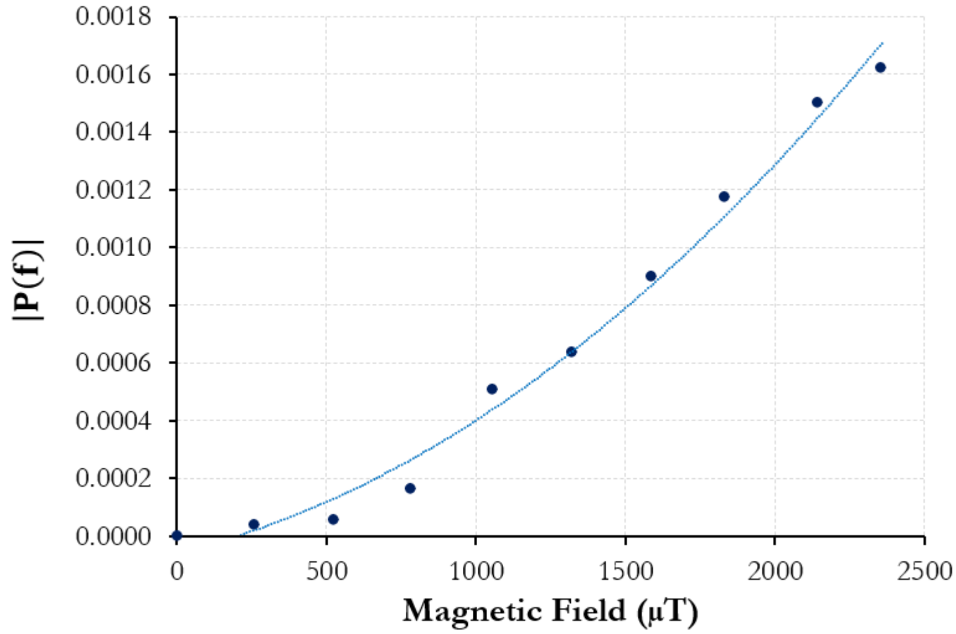

Figure 8-2: Submicron nickel inclusion fiber 340 Hz amplitude spectrum intensity vs 170 Hz AC magnetic field amplitude.

The response at 340Hz is comparatively higher than that at 200Hz for the 170 and 100 Hz driving frequency tests respectively which appears to result from the magneto strictive ribbon resonating. Further testing at a 170 Hz driving frequency gave the same result of a higher comparative response for a given field strength.

From prior investigation, the two-nickel wire multi-material fiber as shown in the SEM image from Figure 5-1, was used in a magnetic field response step test to compare to that of the submicron nickel inclusion sensing fiber. The FFT response amplitude spectrum is shown in Figure 8-3. The amplitude response is larger than that of the submicron sample which is to be expected considering the much higher volume fraction of nickel. Other materials were also studied to look at different sensitivity ranges.

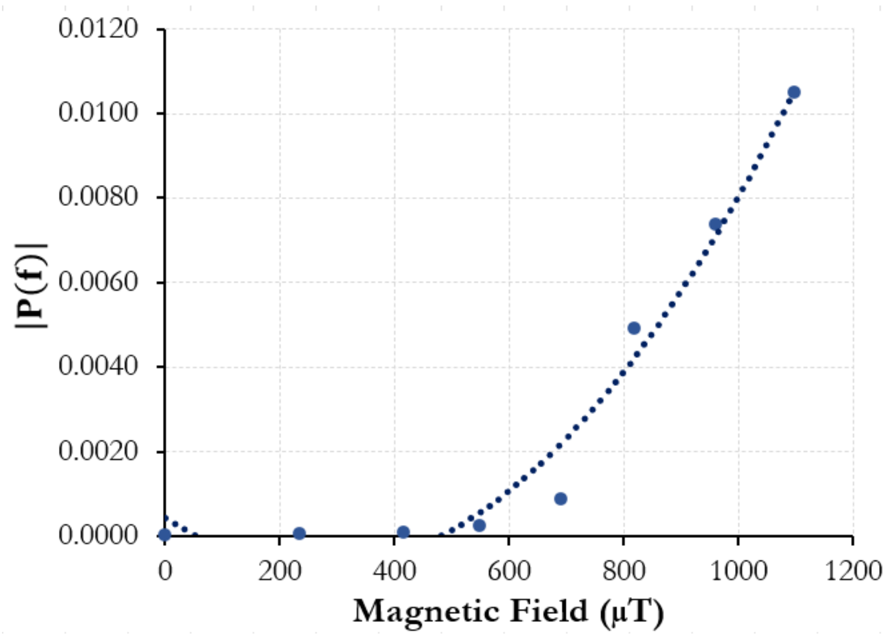

Figure 8-3: 10-micron 2-wire nickel fiber 200 Hz amplitude spectrum intensity vs 100 Hz AC magnetic field amplitude.

A fiber sensor was made using the same method as with the submicron inclusion nickel sample but instead with the alloy galfenol. Galfenol is a ferromagnetic alloy composed of gallium and iron. It is specifically designed for a high strain response to magnetic fields around an order of magnitude higher than that of pure iron. This response is more receptive at larger field densities. Upon testing the galfenol fiber sensor, it did not respond significantly until field strengths of 1000 μT were achieved as shown in Figure 8-4. The strain response appears to exponentially rise as the magnetic field strength is increased past this response threshold with a higher FFT intensity beyond 2000 μT. The magnetostrictive behavior of galfenol matches the higher gradient of the intensity response curve.

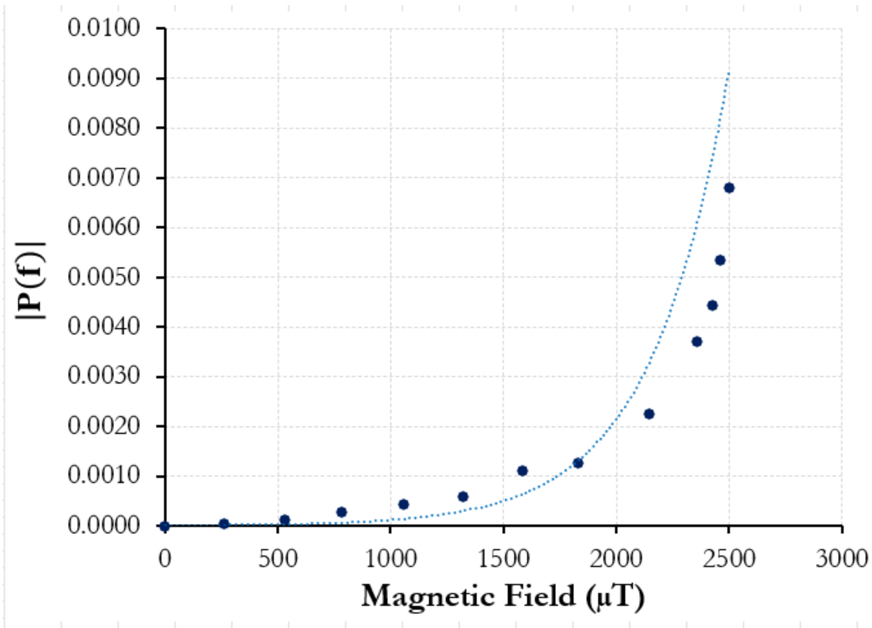

Figure 8-4: Submicron galfenol inclusion fiber 72 Hz amplitude spectrum intensity vs 36 Hz AC magnetic field amplitude.

Normally, the nickel wire sensor begins to become saturated at this strength. The altered response demonstrates that this method of producing magnetic fiber sensors has capabilities of looking at various field strength ranges by changing the material used in the draw.

9. Analysis MetGlas Inclusion Multi-material Fiber Sensor Data

The response of the sensing fiber with one MetGlas® cladding wire was assessed before and after magnetic annealing to evaluate the performance improvement associated with magnetic domain alignment. The sensor response upon exposure to a 100 Hz AC magnetic field was evaluated upon performing the FFT of the measured dynamic strain, as shown in Figure 9-1.

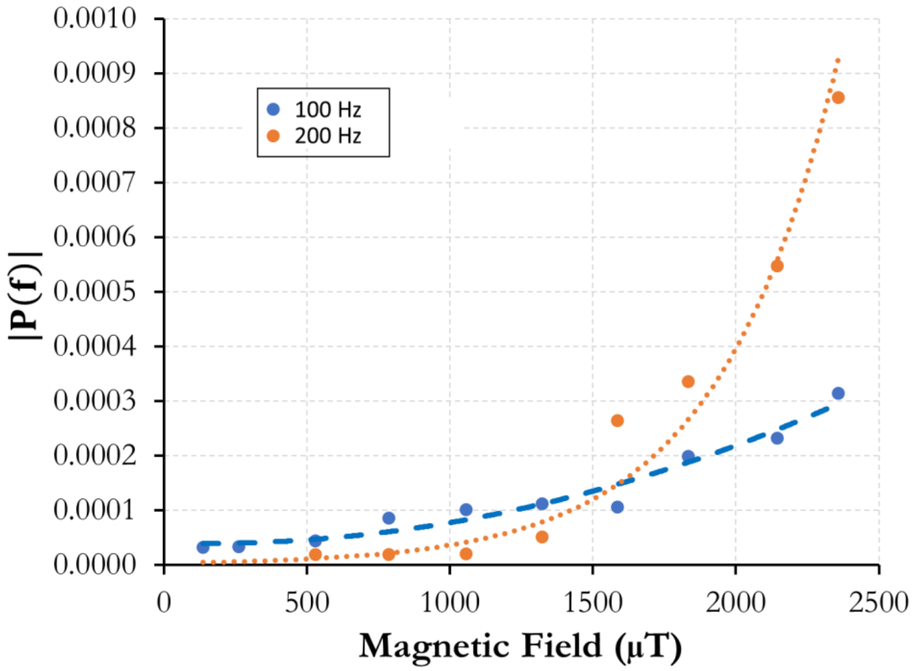

Figure 9-1: 1-wire MetGlas fiber 200 and 100 Hz amplitude spectrum intensity vs 100 Hz AC magnetic field amplitude.

At lower fields, the driving frequency (100 Hz) was dominant, but as the AC magnetic field amplitude is increased, the largest strain response was found at double the driving frequency (200 Hz). This follows the magnetostrictive behavior described in the background section. As shown in Figure 9-1, the 200 Hz curve passes the 100 Hz intensity curve at ~1250 μT. The driving frequency signal at low fields is still present and shows a much smoother initial curve compared to the doubled frequency where the low field trend does not change much from the noise floor of the FFT signal. It is surmised that occurs due to ambient magnetic fields or inconsistencies with the AC voltage signal. At low applied magnetic fields, ambient magnetic signals can act as an offset that precludes the smaller magnetic field amplitudes from crossing the zero point. As such, the frequency of the strain response matches the driving frequency.

Upon magnetic annealing, the magnetic response of the sensing fiber with the one cladding wire was also evaluated upon exposure to an AC magnetic field with 100 Hz driving frequency. As shown in Figure 9-2, an improvement in sensors response is not observed at magnetic field strengths below approximately 750 μT.

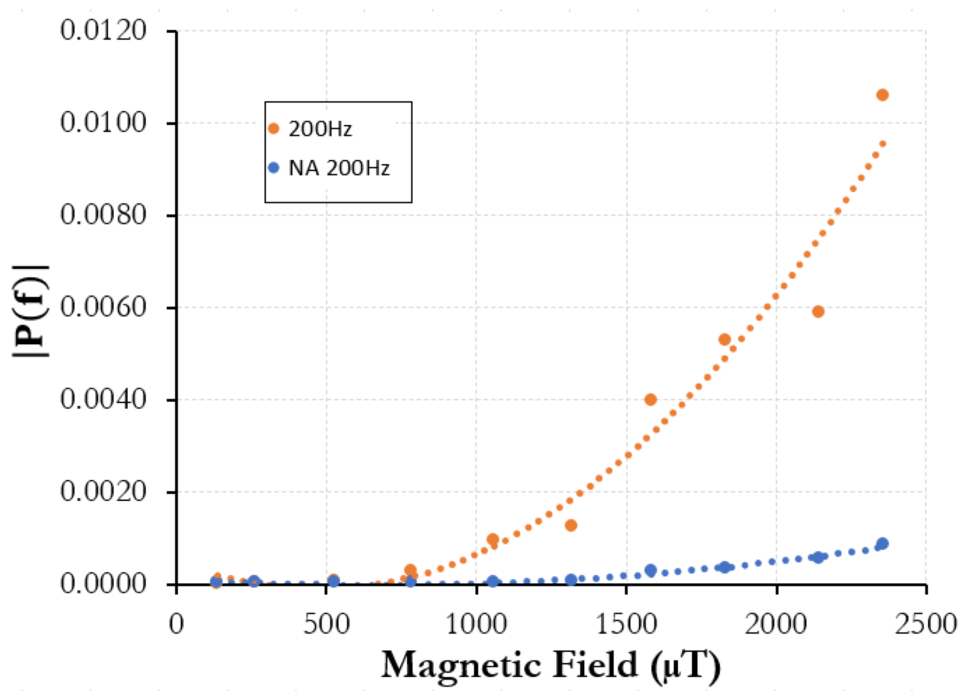

Figure 9-2: 1-wire annealed and non-annealed MetGlas fiber 200 Hz amplitude spectrum intensity vs 100 Hz AC magnetic field amplitude.

This implies that the MetGlas® inside the fiber sensor is approaching saturation of the magnetostriction. Upon increasing the AC magnetic field, the magnetic domains are allowed to move with a larger range of motion and in turn create a stronger strain response and resultant intensity measurement. At the largest field measured (2358 μT), the strain response FFT intensity was almost an order of magnitude greater than that of the sample before it was annealed. Thus, magnetic annealing can be done to increase the relative magnetic sensing resolution for the fiber sensor at higher field strengths, as compared to the pristine condition.

The magnetic response of a sensing fiber with two MetGlas® cladding wires was tested to evaluate the effect of adding more magnetostrictive material in the fiber cladding. The addition of a second MetGlas® cladding wire yielded a significant improvement in sensor response upon exposure to weaker AC magnetic fields with a 100 Hz driving frequency. As shown in Figure 9-3, the minimum detectable fields were two orders of magnitude smaller than that observed for the single cladding wire sample. As anticipated, the dynamic strain was only observed at the driving frequency. A minimum detectable magnetic field strength of ~500 nT was demonstrated, as compared to ~50 μT for the single cladding wire. sample. It is surmised that the increase in the volume of magnetostrictive material in the fiber cladding resulted in greater strain transfer to the fiber, and in turn, better sensitivity. However, with inconsistencies in the draw process and potentially the fiber sensors themselves, other factors could influence the effectiveness of individual fiber samples and more work needs to be done to evaluate and characterize the multi-material fiber magnetic sensors. The double wire MetGlas inclusion sensor was the best performing sample in terms of minimum sensitivity compared to any of the afore tested fiber sensors and provides promise moving forward for further improvement.

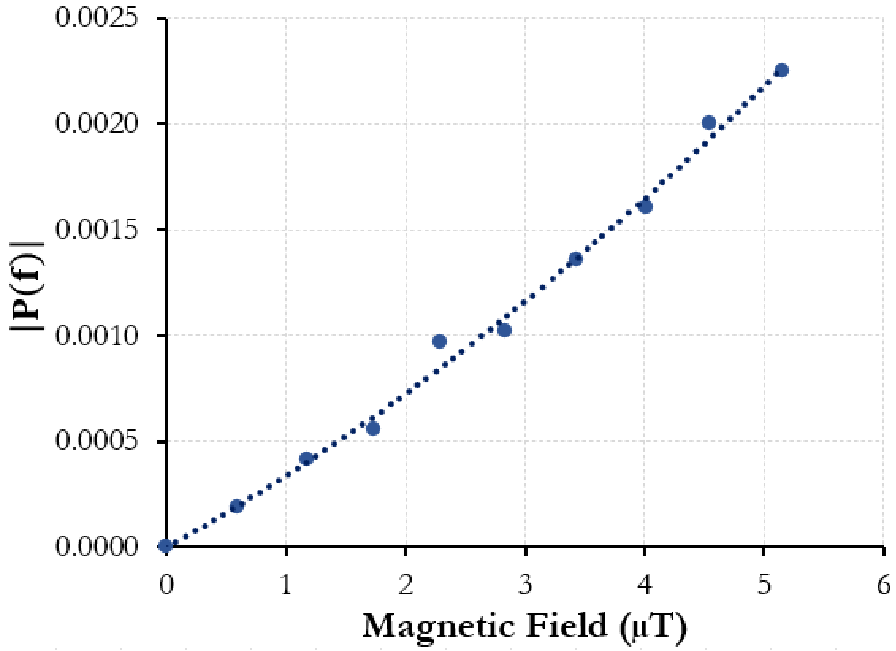

Figure 9-3: 2-wire MetGlas fiber 100 Hz amplitude spectrum intensity vs 100 Hz AC magnetic field amplitude.

10. Magnetostrictive Ribbon Testing

In the sections discussed above, different magnetostrictive wires and wire distributions are studied for a multi-material optical fiber magnetic sensor. Various material substitutions are used to look at different field ranges such as MetGlas for smaller magnetic fields or galfenol alloy for larger fields and a higher resultant strain response. Wire inclusion sizes began on the order of a few micrometers with only one or two wires but were then added in with smaller diameters and significantly more magnetostrictive inclusions. This allowed for the ability to splice the sensor and bypass the manual alignment but with the concession of lower sensitivity. A different sensing arrangement was proposed using standard SMF acoustic sensors in combination with magnetostrictive ribbon. This setup allows for normal splicing as the addition of magnetostrictive materials is outside of the fiber. A significantly higher volume fraction of metal is able to be used for the sensing system giving potential for a better intensity signal measurement.

11. Magnetostrictive Ribbon and Acoustic Sensing Optical Fiber

To test the magnetostrictive response of the ribbon and strain transfer to the acoustic fiber, the same 2-meter air core solenoid and function generator / amplifier setup was used as in the earlier tests. A 1.75 m long ribbon of MetGlas (identical to the material drawn into the multi-material fiber MetGlas inclusion samples) was placed in the air core solenoid with a standard acoustic FBG based fiber sensor pulled through the solenoid and placed directly on top of the ribbon. This setup is shown in Figure 11-1.

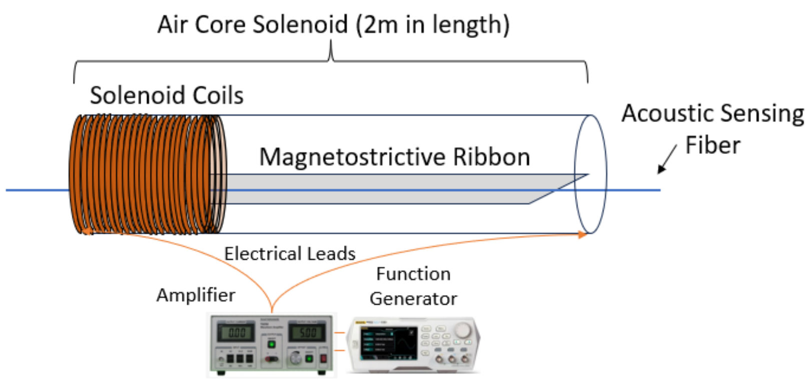

Figure 11-1: Acoustic sensing fiber and magnetostrictive ribbon experimental setup.

As in the other magnetic field sensor calibration tests, a frequency was chosen, and the voltage across the air core solenoid was increased as measurements were taken. The AC magnetic field amplitude was recorded at each step of the recorded measurements. Figure 11-2 shows the intensity response at 200 Hz of the acoustic fiber from 0 to around 20 μT for a 100Hz driving frequency.

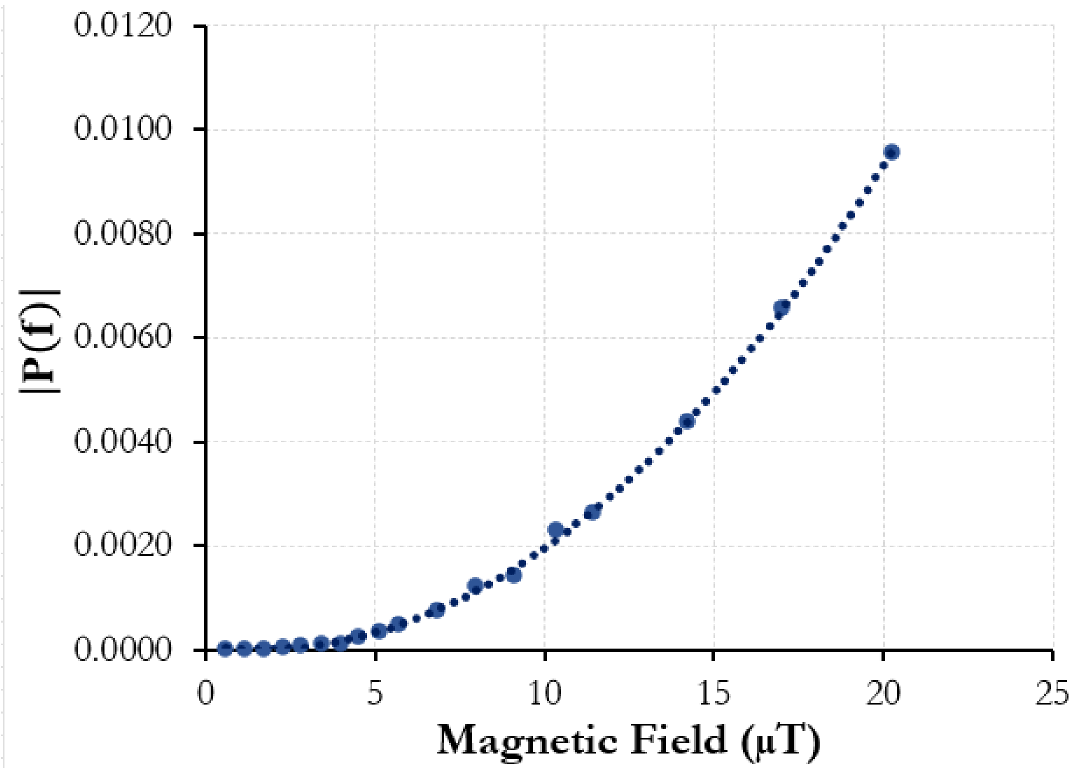

Figure 11-2: Acoustic sensing fiber and MetGlas ribbon 200 Hz amplitude spectrum intensity vs 100 Hz AC magnetic field amplitude.

Compared to the relative intensity responses looked at in the earlier chapters and specifically the MetGlas multi-material fiber response, the ribbon and acoustic sensing fiber is more volatile in response. The orientation and positioning of the fiber on the ribbon greatly affects the resultant intensity from the acoustic fiber. Additionally, a variety of harmonics show up outside of just the driving frequency and magnetostrictive doubled peak as shown in the amplitude spectrum in Figure 11-3.

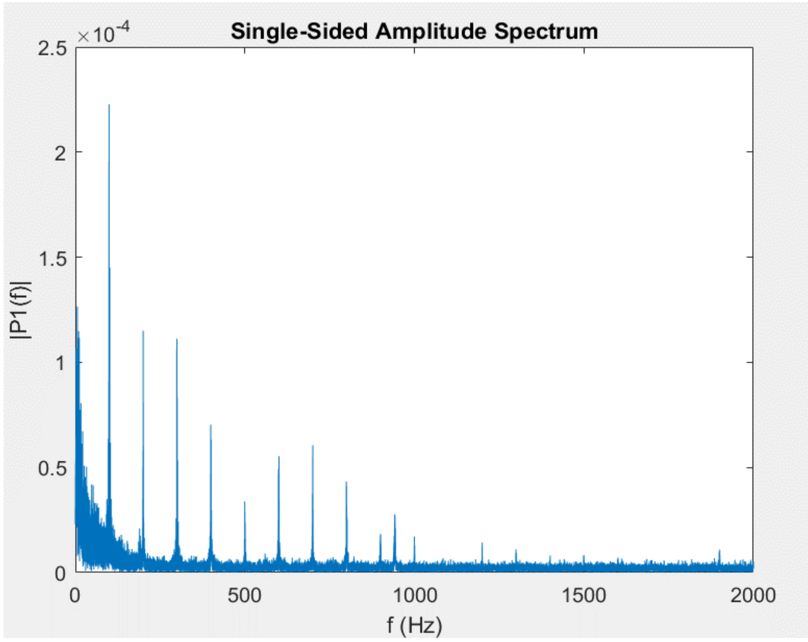

Figure 11-3: Acoustic sensing fiber and MetGlas ribbon amplitude spectrum response at 3.43 µT.

Taken at 3.43 µT, the 100 Hz peak (driving frequency) is 2.25E-4 for the ribbon while the MetGlas multi-material sample at 5.71 µT had a response of 4E-3 in Figure 9-3 for 100 Hz. Even though the applied field was 66% higher for the multi-material sensor, the respective response was over an order of magnitude higher compared to that of the ribbon variation. However, as the field is increased, this discrepancy flips, and higher frequency harmonics start to come into play. In Figure 11-4, the highest individual peak is at 300 Hz. The FFT intensity response is taken at 28.56 µT. Peaks begin to show up along integer intervals of the driving frequency.

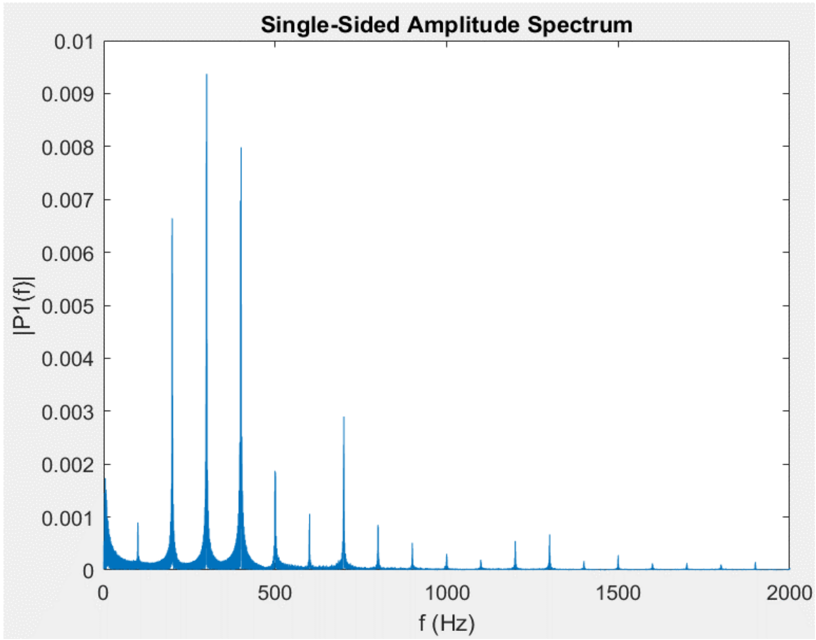

Figure 11-4: Acoustic sensing fiber and MetGlas ribbon amplitude spectrum response at 28.56 μT.

Among the multi-material fiber sensors, the strain response starts to saturate around 20 μT but as the voltage is continually increased with the magnetostrictive ribbon, the response still scales and can even be heard audibly depending on what frequency is being emitted from the waveform generator. This makes the acoustic sensing fiber and ribbon setup ideal for applications where higher fields are present and there is more available space for deployment as the ribbon makes the dual element sensor slightly bulkier than just the multi-material sensor. However, fiber drawing is significantly easier as standard acoustic sensing fiber is commercially available, fast to produce as well as inexpensive.

Moving forward with improving magnetic sensing ability in fiber optics, there are multiple areas and paths to be further researched and studied. One way of doing this that has already been discussed throughout this work is changing and experimenting with the magnetostrictive materials used for the sensing system. MetGlas was used for its strain response at very low AC magnetic fields, while galfenol alloy was for improving the overall strain response intensity even at larger field strengths. Nickel was used as it is inexpensive and easiest to work within the fiber draw process. All the different materials used throughout have their drawbacks as well as their benefits. Optimizing this in some combination or looking at new alloys altogether could provide new insights towards improved magnetic sensing either through sensitivity improvements, better reliability, easier manufacturing, etc. More work needs to be done to look at successfully adding inclusions of this material into an optical fiber sensor to study this further.

The background section looks at the general magnetostriction curve for applicable materials plotting strain response versus an applied magnetic field in Figure 2-2. It would be valuable to collect small incremental data with the magnetic sensing fiber samples to mathematically establish a magnetostriction curve for a given field range up until saturation. This would allow easy predictions and modeling of the material and sensor for determining effective sensitivity as well effects of adding a bias.

After finding success in the MetGlas ribbon, the research group was able to acquire another specifically engineered magnetostrictive alloy coined Vitrovac. Similar to MetGlas, the metal is designed to have a substantial strain response at low field strengths. As in the MetGlas ribbon and acoustic fiber testing setup, the acquired Vitrovac metal ribbon was used to run an identical test to look for potential improvements strain response/sensitivity. In Figure 11-5, the FFT intensity is plotted against an increasing AC magnetic field amplitude for the acoustic sensing fiber placed on top of the Vitrovac ribbon in the aircore solenoid. The amplitude ranges from 67 nT to just over 300. While the setup allowed for the fiber/ribbon response to go lower, the magnetic probe that was used to measure the corresponding magnetic field of the air core solenoid did not have the resolution.

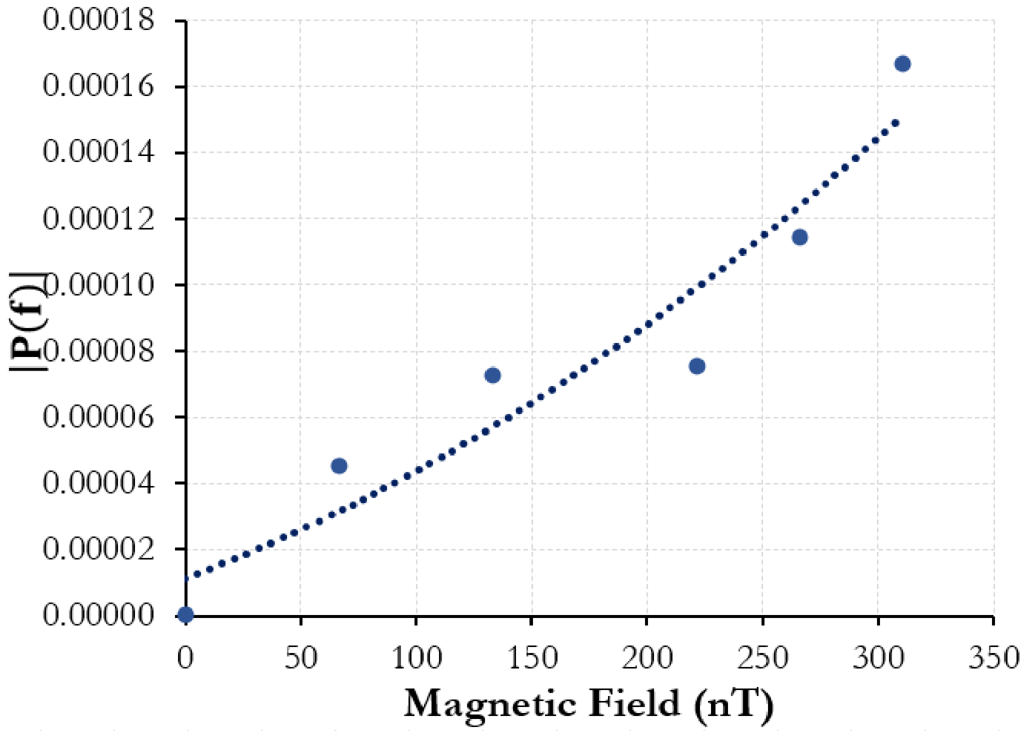

Figure 11-5: Acoustic sensing fiber and Vitrovac ribbon 100 Hz amplitude spectrum intensity vs 100 Hz AC magnetic field amplitude.

The first attempts at drawing the Vitrovac along with the silica fiber failed. However, preliminary data was obtained first in using the initially provided Vitrovac material in ribbon form, to mirror that of the earlier setup with MetGlas and an acoustic sensing fiber. This test yielded a high strain response intensity measurement even at fields on the order of tens of nano-Tesla as shown in Figure 11-5. Looking at the difference in response of using MetGlas in the fiber compared to using an acoustic fiber coupled with MetGlas ribbon, this shows promise for a Vitrovac multi-material fiber sensor. In Figure 11-6, a comparison of the MetGlas ribbon response with the 2-wire MetGlas is shown. At a magnetic field amplitude of 4.5 μT the response of the MetGlas multi-material fiber sensor for a 100 Hz driving frequency has an FFT intensity response almost exactly an order of magnitude higher than that of the acoustic fiber and MetGlas ribbon.

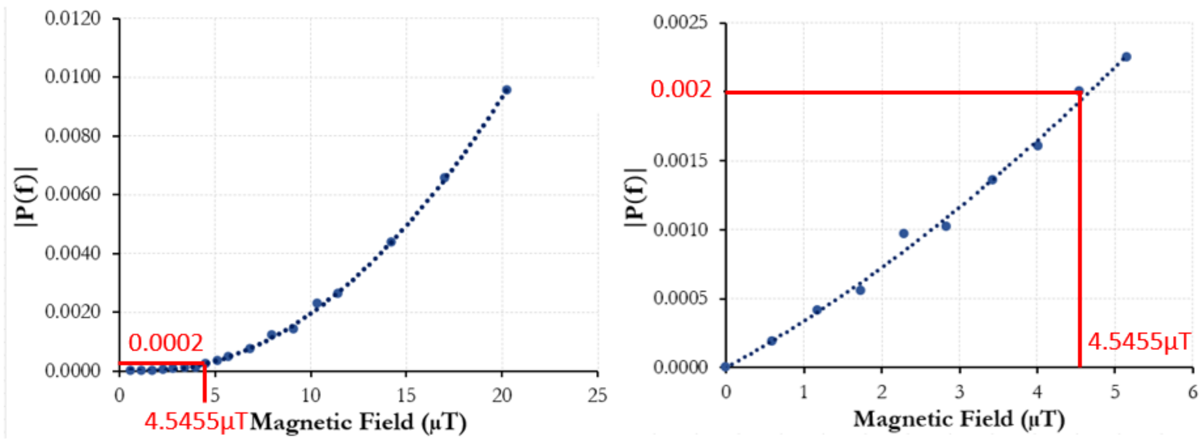

Figure 11-5: Acoustic sensing fiber and MetGlas ribbon 200 Hz amplitude spectrum intensity vs 100 Hz AC magnetic field amplitude and 2-wire MetGlas sensing fiber comparison.

Based on the comparison and extrapolating out, this demonstrates that a fiber sensor with Vitrovac inclusions could yield a fiber with sensing range on the scale of single nanotesla or even picotesla, which has a lot of desirable applications for biomedical research.

Conclusions

In this study, a multi-material fiber optic magnetic sensor was first proposed and tested using 10-micron diameter nickel wires. The initial nickel samples however were only able to detect signals from magnetic field amplitudes of a few hundred micro-Tesla or higher and because of the large size of the inclusion(s), the fibers were not able to be spliced, complicating the initial setup. A new design was proposed to approach this obstacle and shrink the size of the submicron inclusions as well as adding in more of the continuous nickel wires. This addressed the issue of splicing, but with the cost of slightly lower sensitivity. A multi-material magnetic sensing fiber with galfenol alloy inclusions was also fabricated to look at higher magnetic field ranges for better resolution. This was done using the same technique so that the fiber could be spliced.

While using galfenol alloy and nickel as the material for the inclusions showed promising results for magnetic sensing at the micro tesla level, a lot of applications require magnetic sensitivity on the order of nanotesla. Thus, it was proposed to use a new material, MetGlas, specifically engineered to have a substantial magnetostrictive response even at lower field amplitudes. With MetGlas inclusions, FFT peak responses from the data analysis showed the multi-material fiber able to detect field amplitudes as low as 500 nT.

The final testing looked at the future work needed to be done and discussed the introduction of using magnetostrictive ribbon in combination with acoustic sensing fiber. The fiber draw process is often inconsistent and difficult when trying to draw metal inclusion wires inside the cladding of the fiber. Using the material outside of the fiber, the draw process was no longer a challenge allowing for the testing of new materials like Vitrovac. The initial findings from these tests demonstrated potential for even lower sensitivity for using Vitrovac inclusions as opposed to MetGlas.

Optical fiber and the surrounding technology enable the creation of new multi-material fiber-based sensors able to outperform traditional magnetometers because of their robust form and distributed sensing capabilities. This study looks at ways of demonstrating multiple fiber sensors for magnetic field sensing at different field strengths, frequencies, and setup requirements. The success of testing the different fiber samples and noted future work provides insight to further areas and sensor arrangements to be studied for eventual commercial use in down hole or other applications with the desire for distributed sensing across a wide range of magnetic field strengths.

References

[1] Gooneratne, Chinthaka P., Bodong Li, and Timothy E. Moellendick. "Downhole applications of magnetic sensors." Sensors 17.10 (2017): 2384.

[2] Kleiner, Reinhold, et al. "Superconducting quantum interference devices: State of the art and applications." Proceedings of the IEEE 92.10 (2004): 1534-1548.

[3] Liu, Wei, et al. "A new downhole magnetic resonance imaging tool." Microporous and Mesoporous Materials 269 (2018): 97-102.

[4] Avendano, Carolina, et al. "Magnetic characterization of nanoparticles designed for use as contrast agents for downhole measurements." SPE International Oilfield Nanotechnology Conference and Exhibition. SPE, 2012.

[5] Neal, Jack and Chris Krohn. "Higher Resolution Subsurface Imaging." Journal of Petroleum Technology 64, no. 03 (2012): 44-53.

[6] U.S. Department of Energy, Controlling Subsurface Fractures and Fluid Flow: A Basic Research Agenda, DOE Roundtable Report, May 22, 2015 Germantown, MD. Available at: http://science.energy.gov/~/media/bes/pdf/reports/2015/BES_CSFFF_rtp.pdf.

[7] M Razavy, Generation of harmonics in a waveguide with moving boundaries, Wave Motion, Volume 20, Issue 4, 1994, Pages 397-406, ISSN 0165-2125, https://doi.org/10.1016/0165-2125(94) 90022-1

[8] Beer, Rudolfo, Paulo Roberto Alves Netto, Ajay Nalonnil, Sebastian Thum, Badarinadh Vissapragada, Ping Zhang, David Alumbaugh, Laurence Reynolds, Mark McCallum and Kim Gunn Maver. "Improved Formation Imaging of the Interwell Space with Deep Reading

Technologies." In SPWLA 51st Annual Logging Symposium: Society of Petrophysicists and Well-Log Analysts, 2010.

[9] Katterbauer, Klemens, Ibrahim Hoteit and Shuyu Sun. "Synergizing Crosswell Seismic and Electromagnetic Techniques for Enhancing Reservoir Characterization." SPE Journal, (2015).

[10] Murray, Christopher J, George V Last and Michael J Truex. Review of Geophysical Techniques to Define the Spatial Distribution of Subsurface Properties or Contaminants: Pacific Northwest National Laboratory, 2005.

[11] Sava, P, A Revil and M Karaoulis. "High Definition Cross-Well Electrical Resistivity Imaging Using Seismoelectric Focusing and Image-Guided Inversion." Geophysical Journal International 198, no. 2 (2014): 880-894.

[12] Harris, Jerry M and Robert T Langan. "Crosswell Seismic Profiling: Principle to Applications." Search and Discovery Article 40030, (2001): 2001.

[13] Wilt, MJ, DL Alumbaugh, HF Morrison, A Becker, Ki Ha Lee and M Deszcz-Pan. "Crosswell Electromagnetic Tomography: System Design Considerations and Field Results." Geophysics 60, no. 3 (1995): 871-885.

[14] Chang, Chung, David Hoyle, Shinichi Watanabe, Richard Coates, Michael Kane, Kevin Dodds, Cengiz Esmersoy and Jerome Foreman. "Localized Maps of the Subsurface." Geophysics

[15] U.S. Department of Energy Subsurface Technology and Engineering RD&D Crosscutting Team. Subsurface Control for a Safe and Effective Energy Future, http://energy.gov/downloads/subter-crosscut-white-paper.

[16] U.S. Department of Energy, QUADRENNIAL TECHNOLOGY REVIEW: AN ASSESSMENT OF ENERGY TECHNOLOGIES AND RESEARCH OPPORTUNITIES, Chapter 1, September 2015 http://energy.gov/sites/prod/files/2015/09/f26/QTR2015-Challenges.pdf

[17] Phillips, Benjamin R, John Ziagos, Hildigunnur Thorsteinsson and Eric Hass. "A Roadmap for Strategic Development of Geothermal Exploration Technologies." In Proceedings, Thirty-Eighth Workshop on Geothermal Reservoir Engineering, 11-13, 2013

[18] U.S. Department of Energy, SubTER AGU Townhall, TH25I, December 15th, 2015.

http://energy.gov/sites/prod/files/2016/01/f29/AGU%20SubTER%20Townhall%202015_0.pdf

[19] U.S. Department of Energy, Carbon Storage Technology Program Plan, December 2014. Available at: http://www.netl.doe.gov/File%20Library/Research/Coal/carbon-storage/Program-Plan-Carbon-Storage.pdf.

[20] Arscott, R Lyn, Charles Fairhurst and Larry Lake. "Grand Challenges for Earth Resources Engineering." Journal of Petroleum Technology 64, no. 06 (2012): 66-71.

[21] U.S. Department of Energy, Controlling Subsurface Fractures and Fluid Flow: A Basic Research Agenda, DOE Roundtable Report, May 22, 2015 Germantown, MD. Available at: http://science.energy.gov/~/media/bes/pdf/reports/2015/BES_CSFFF_rtp.pdf.

[22] Beer, Rudolfo, Paulo Roberto Alves Netto, Ajay Nalonnil, Sebastian Thum, Badarinadh Vissapragada, Ping Zhang, David Alumbaugh, Laurence Reynolds, Mark McCallum and Kim Gunn Maver. "Improved Formation Imaging of the Interwell Space with Deep Reading

Technologies." In SPWLA 51st Annual Logging Symposium: Society of Petrophysicists and Well-Log Analysts, 2010.

[23] Katterbauer, Klemens, Ibrahim Hoteit and Shuyu Sun. "Synergizing Crosswell Seismic and Electromagnetic Techniques for Enhancing Reservoir Characterization." SPE Journal, (2015).

[24] Murray, Christopher J, George V Last and Michael J Truex. Review of Geophysical Techniques to Define the Spatial Distribution of Subsurface Properties or Contaminants: Pacific Northwest National Laboratory, 2005.

[25] Sava, P, A Revil and M Karaoulis. "High Definition Cross-Well Electrical Resistivity Imaging Using Seismoelectric Focusing and Image-Guided Inversion." Geophysical Journal International 198, no. 2 (2014): 880-894.

[26] Harris, Jerry M and Robert T Langan. "Crosswell Seismic Profiling: Principle to Applications." Search and Discovery Article 40030, (2001): 2001.

[27] Wilt, MJ, DL Alumbaugh, HF Morrison, A Becker, Ki Ha Lee and M Deszcz-Pan. "Crosswell Electromagnetic Tomography: System Design Considerations and Field Results." Geophysics 60, no. 3 (1995): 871-885.

[28] Chang, Chung, David Hoyle, Shinichi Watanabe, Richard Coates, Michael Kane, Kevin Dodds, Cengiz Esmersoy and Jerome Foreman. "Localized Maps of the Subsurface." Geophysics 57, no. 1 (1992): 146-160.

[29] Knapp, Ralph W and Don W Steeples. "High-Resolution Common-Depth-Point Seismic Reflection Profiling: Instrumentation." Geophysics 51, no. 2 (1986): 276-282.

[30] Baihly, Jason, Allen Dutt, Efejera Ejofodomi, Alex Menkhaus, Paul Dickenson, Colin Wilson and Kevin England. "Fiber Optic Revelations from a Multistage Open Hole Lateral Fracturing Treatment." Unconventional Resources Technology Conference (URTEC), 2015.

[31] Homa, D., Y. Liang, and G. Pickrell. "Superconducting fiber." Applied Physics Letters 103, no. 8 (2013).

[32] Hileman, Zachary, et al. "Development of a multimaterial optical fiber for fully distributed magnetic sensing applications." IEEE Sensors Letters 6.1 (2021): 1-4.

[33] Qi B, Pickrell GR, Zhang P, Duan Y, Peng W, Xu J, Huang Z, Deng J, Xiao H, Wang Z, Huo W. Fiber optic pressure and temperature sensors for oil down hole application. InFiber Optic Sensor Technology and Applications 2001 2002 Feb 14 (Vol. 4578, pp. 182-190). SPIE

[34] L. Minggan, W. Zhang, W. Huang, X. Xi, Optical Fiber Magnetic Field Sensors Based on 3 × 3 Coupler and Iron-Based Amorphous Nanocrystalline Ribbons, Sensors 23(5) (2023) 2530.

[35] K. Rao, Temperature and annealing dependencies of magnetostriction constant in a Co-rich zero-magnetostrictive metallic glass, IEEE Transactions on Magnetics 22(5) (1986) 451-453.